

Article

Switching Power Suppliers Noise Reduction in Ultrasound Doppler Fluid Measurements

Stefano Ricci 

Information Engineering Department (DINFO), University of Florence, 50139 Florence, Italy; stefano.ricci@unifi.it; Tel.: +39-055-275-8585

Received: 11 March 2019; Accepted: 8 April 2019; Published: 11 April 2019



Abstract: Ultrasound Doppler techniques are widely employed in detecting the velocity of moving fluids both in medical and industrial applications. Echo Doppler electronics systems include a highly sensitive front-end suitable to processing the very low power ultrasound echoes received by the transducer. Moreover, the front-end input bandwidth typically ranges between 100 kHz and 10 MHz, which is the same frequency range where modern switching regulators work. Thus, the front-end is particularly prone to the noise produced by the suppliers that power the board itself. Electromagnetic interference (EMI) filters and spread-spectrum modulation of the switching regulator frequency help, but the results are often not optimal, and unacceptable artifacts are visible in the Doppler spectrum. In this paper a spread-spectrum modulation is proposed that concentrates the switching noise in the low-frequency range of the Doppler spectrum (e.g., 0–100 Hz). This range is removed by the high-pass clutter filter normally used in velocity Doppler investigations, thus switching noise and artifacts are eliminated. The method is verified through mathematical simulations and tested in measurements carried out with a research Doppler system. An example is presented in which the artifacts present during the investigation of a 0.4-m/s flow in a 25.4-mm diameter pipe are effectively removed by the proposed method.

Keywords: EMI reduction; switching power regulator; ultrasounds; Doppler measurement; flow measurement

1. Introduction

Ultrasound Doppler is employed in several medical and industrial applications for fluid velocity investigation. Clinical echographs exploit echo Doppler for acquiring important information about how blood moves in arteries [1–3], and industries employ similar techniques for detecting the velocity profile of fluids flowing in pipes. In this case, the final application can be, for example, accurate volume flow detection or rheological fluid characterization [4–6].

The echo signal backscattered from the particles dispersed in the fluid (e.g., erythrocytes in the blood or powders in water) is quite weak. This issue is particularly severe in industrial applications where attenuating fluids or suspensions flow in pipes with large diameters. The ultrasound system should be equipped with a very sensitive front-end receiver, which, in turn, is prone to pick up electronic noise from the system itself.

Power switching regulators are widely used for their superior efficiency [7], but unfortunately they introduce a high noise at the switching frequency and its harmonics. Moreover, the working frequency range of modern switching regulators starts from hundreds of kHz and rises up to some MHz. This is the range where ultrasound applications in fluids work as well [8], making their susceptibility even more critical. If a Doppler system is affected by this noise, the Doppler spectrum (i.e., the spectrum reporting Doppler frequency shifts related to the moving fluid) is affected by unacceptable

artifacts. Filters are used to mitigate the problem [9], but, although they help, their employment is rarely resolute.

Spread spectrum techniques are widely used for controlling the noise produced by circuit commutations, as well as being effectively applied for mitigating the noise produced by power switching regulators [10–12]. In the spread spectrum approach, the power switcher is synchronized to a frequency that is modulated according to a given temporal trend, which in most cases is triangular-shaped [10]. The overall noise power does not change, but the spectral peak value is reduced from being distributed over a wider range of frequencies. This technique helps an electronics system to be compliant to electromagnetic interference (EMI) tests for certification, which require the noise to be under a given spectral density distribution. A notable example is CISPR 11 normative, which applies to industrial and medical equipment [13]. Electronic Doppler systems benefit from the spread spectrum technique as well. However, as shown later in this paper, artifacts in the Doppler spectrum can still be present even when power switching regulators are modulated through the spread spectrum technique.

In this paper we present a spread spectrum method that exploits the particular features of Doppler data processing for effectively cancelling the power switching noise in the Doppler spectrum. This is achieved by synchronizing the power switching regulator to a signal with triangular frequency modulation whose parameters are tuned to the Doppler investigation running on the system at that moment. Thanks to the particular tuning, the noise is concentrated in the specific region of the Doppler spectrum, which is removed by the clutter filter [14]—a high-pass filter normally used to cut the high contribution of still obstacles (e.g., pipe walls) or slowly moving media (e.g., tissue around an artery).

The paper proceeds by providing a mathematical model of the switching noise and calculating how it is modified when processed through the elaboration chain of the Doppler data. This model is applied to the noise signal picked up by the sensitive input of a Doppler system in Section 3, where the proposed method is described. Section 4 describes the method implementation in a Doppler system designed for rheological industrial applications [15]. And finally, in Section 5, the method is first verified with MATLAB (The MathWorks, Natick, MA, USA) simulations, then tested on the Doppler system described in Section 4. A final experiment shows the effectiveness of the method with the system connected to a flow-rig where a 0.4-m/s fluid is pumped in a 25.4-mm industrial pipe.

2. Mathematical Model of Switching Noise and Doppler Signal Elaboration

2.1. Signal Model of Simple Mono-Frequency and Triangular-Modulated Square Pulses

The noise produced by the power switching regulator is mainly due to the commutation of the MOSFET switch. The noise can be roughly modeled by a periodic pulse synchronous to the switching frequency, which can be fixed or can follow a specific profile like in the spread spectrum approach. In this section, a mathematical model of the noise is calculated for when the switching frequency is constant and has a periodical triangular trend in time. It is convenient to define the functions:

$$\text{TRI}(x) = \begin{cases} 2x & x \in]0, 0.5] \\ 2 - 2x & x \in]0.5, 1] \\ 0 & x \notin]0, 1] \end{cases} \quad (1)$$

$$\prod_T(x) = \begin{cases} 1 & x \in]-\frac{T}{2}; \frac{T}{2}] \\ 0 & x \notin]-\frac{T}{2}; \frac{T}{2}] \end{cases} \quad (2)$$

$$\text{TRIP}(x) = \sum_{n=-\infty}^{+\infty} \text{TRI}(x - n); n \in \mathcal{N} \quad (3)$$

$$\text{RECTp}(x) = \sum_{n=-\infty}^{+\infty} \left(\prod_T(x - nT_m) \right); n \in \mathcal{N} \tag{4}$$

TRI(x) represents a triangle of height 1 and base 1, and TRIp(x) is the periodic extension of period 1; $\prod_T(x)$ represents a pulse of duration T, and RECTp(x) is the periodic expansion of period T_m with duty cycle $\frac{T}{T_m}$. Starting from Equation (4), a periodic pulse of constant frequency F_M is simply represented as

$$s_M(t) = \text{RECTp}(F_M \times t) \tag{5}$$

Let us focus now on the model of a noise modulated according to a triangular frequency trend. The triangular temporal trend $f_T(t)$ of the modulation frequency is

$$f_T(t) = F_m + (F_M - F_m) \times \text{TRIp}(F_{Mod} \times t) \tag{6}$$

where F_M and F_m are the maximum and minimum frequencies, respectively, of the frequency range, and F_{Mod} is the frequency of the modulation (i.e., the rate of repetition of the triangular shape).

A periodic pulse of instantaneous frequency $f(t)$ is represented by $s(t) = \text{RECTp}(\int f(\delta)d\delta)$. Thus, the noise pulse modulated by a triangular frequency is

$$s_T(t) = \text{RECTp}(\varnothing(t)); \tag{7a}$$

$$\varnothing(t) = \int_0^t [F_m + (F_M - F_m) \times \text{TRIp}(F_{Mod} \times \delta)]d\delta \tag{7b}$$

where $\varnothing(t)$ is the summation of the function $f_T(t)$ that is periodic of period $\frac{1}{F_{Mod}}$. It is convenient to subdivide the summation into a part, $\varnothing_A(N)$, composed of an integer number N of complete triangular periods, and another part, $\varnothing_B(t)$, that includes the fractional section of the last period:

$$\varnothing(t) = \varnothing_A(N) + \varnothing_B(t) \quad N = \text{INT}(t \times F_{Mod}) \tag{8a}$$

$$\varnothing_A(N) = \int_0^{\frac{N}{F_{Mod}}} [F_m + (F_M - F_m) \times \text{TRIp}(F_{Mod} \times \delta)]d\delta \tag{8b}$$

$$\varnothing_B(t) = \int_{\frac{N}{F_{Mod}}}^t [F_m + (F_M - F_m) \times \text{TRIp}(F_{Mod} \times \delta)]d\delta; \quad \frac{N}{F_{Mod}} < t < \frac{N+1}{F_{Mod}} \tag{8c}$$

where INT(x) is the lower positive integer value with respect to x. Since TRI(x) is a triangle of area $\frac{1}{2}$, it follows that

$$\int_0^{\frac{1}{F_{Mod}}} \text{TRIp}(F_{Mod} \times \delta)d\delta = \frac{1}{2 \times F_{Mod}} \tag{9}$$

And then, after some simple mathematical steps Equation (8b) can be written as:

$$\varnothing_A(N) = \frac{N}{F_{Mod}} \left(\frac{1}{2}F_M + \frac{1}{2}F_m \right) \tag{10}$$

Using Equations (8a), (8c), and (10), we have

$$\varnothing(t) = \frac{N}{F_{Mod}} \left(\frac{1}{2}F_M + \frac{1}{2}F_m \right) + \int_{\frac{N}{F_{Mod}}}^t [F_m + (F_M - F_m) \times \text{TRIp}(F_{Mod} \times \delta)]d\delta \tag{11}$$

Equation (11), substituted in Equation (7a), represents a model of the noise produced by the switching regulator when synchronized to a frequency with triangular modulation between F_m and F_M .

2.2. Data Elaboration in a Doppler System

A pulse-wave Doppler system investigates the velocity distribution in a fluid by transmitting a burst of ultrasounds of frequency F_T every pulse repetition interval (PRI) [1]. The ultrasonic burst travels in the medium at velocity c , and when it encounters a scatterer, part of its energy is reflected towards the transducer. If the scatterer moves at velocity v , the echoes from subsequent transmissions are returned from slightly different positions. Thus, they are affected by a phase shift. The echo signal sampled at the same distance from the transducer and from subsequent PRIs presents a phase variation that corresponds to the frequency f_v described by the Doppler equation: $f_v = \frac{v}{c} F_T \cos(\theta)$, where θ is the angle between the direction of the ultrasound wave and the scatterer velocity, and the factor 2 in front of the formula accounts for the back and forth path the burst travels between the transducer and the target.

The weak echoes, possibly overlapped to noise, are received by the transducer, amplified, filtered and sampled at rate $F_c = \frac{1}{T_c}$. The elaboration of a signal in a Doppler system is detailed, for example, in [1]. In this section the elaboration is briefly summarized and adapted to the case of interest. The switching-regulator produces a periodic noise signal whose harmonics $s_{SWn} = \sin(2\pi f_{SWn}t)$ have the frequency

$$f_{SWn} = \begin{cases} f_{SW0} & n = 0 \\ (n + 1) \times f_{SW0} & n > 0 \end{cases} \quad (12)$$

The stream of sampled data is subdivided in PRI sections of length $T_{Pri} = k_M \times T_c$. This process can be expressed by considering the signal sampled at time $t = k \times T_c + l \times T_{Pri}$, and stored in the bidimensional matrix $s_{SWn}(k, l)$. The row index, k , ranges in $0 < k < k_M$, while the column index, l , counts the PRIs. In this notation, the k -index represents the “depth” (i.e., the distance from the transducer). Data sampled at the same k behave to the same depth, and thus are affected by the phase shift described above, which can be detected by a spectral analysis along the l -index. Details follow.

It is convenient to express the harmonics in the complex form

$$s_{SWn}(k, l) = e^{i2\pi f_{SWn}(kT_c + lT_{Pri})} \quad (13)$$

where $i = \sqrt{-1}$. The signal segments stored along the columns of the matrix are coherently demodulated [16] at frequency f_d , which typically corresponds to the frequency of the transmission burst. This operation is performed by multiplying the signal for the complex sequence $e^{-i2\pi f_d k T_c}$ and then applying a low-pass filter with cut-off frequency f_{LP} . f_{LP} is typically adapted to the bandwidth of the transducer. After the demodulation, the signal is

$$s_{SWDn}(k, l) = W(f_{SWn}) \times A(k) \times e^{i2\pi f_{SWn}(lT_{Pri})} \quad (14)$$

where $A(k)$ is the incremental phase shift due to $f_{SWn} - f_d$, and $W(f_{SW0})$ accounts for the low-pass filter:

$$W(f_{SWn}) = \begin{cases} 1 & |f_{SWn} - f_d| < f_{LP} \\ 0 & |f_{SWn} - f_d| > f_{LP} \end{cases} \quad (15a)$$

$$A(k) = e^{2\pi i(f_{SWn} - f_d)kT_c} \quad (15b)$$

Note that $A(k)$ depends only on the row index and has unity magnitude. The sequence in Equation (14), read for columns (i.e., by varying the index l with the k constant), represents the original noise harmonics of Equation (12) reported in a complex form, with the phase rotated by $(f_{SWn} - f_d)kT_c$. In other words, the magnitude and frequency of the harmonics of the input noise signal sampled along the l -index is not changed by the elaboration, provided that such harmonics are in the range $f_d - f_{LP} < f_{SWn} < f_d + f_{LP}$ (i.e., they go through the low-pass filter represented in Equation (15a)).

The elaboration proceeds by considering the data sequence along the l -index with the k constant (in other words, the sequences that collect data from the same depth in the fluid). A high-pass filter (anti-clutter) [14] is applied to the signal matrix along the l -index, then the data sequence is processed for spectral estimation with fast Fourier transform (FFT) [17] or more sophisticated adaptive estimators [18–20]. In the last step, the spectral power is calculated. The final spectral Doppler matrix represents an intuitive picture of the flow profile in the pipe. Its rows report the Doppler shifts, which are proportional to the flow velocity; the columns report the depths inside the pipe. The harmonics of the noise, if present, produce annoying artifacts.

3. Method

3.1. Constant Frequency Noise

In the trivial case of constant switching frequency, the noise is effectively removed by the high-pass clutter filter when the frequency and phase of the input signal are selected, so that its harmonics are a multiple of $1/T_{Pri}$ (i.e., $F_M = K/T_{Pri}$). In fact, in this hypothesis, the pulse Equation (5) is written as

$$s_M(t) = \text{RECTp}\left(\frac{K}{T_{Pri}} \times t\right) \quad K \in \mathcal{N} \tag{16}$$

The lowest harmonic has the frequency $f_{SW0} = K/T_{Pri}$, the others have the frequency $f_{SWn} = nK/T_{Pri}$. Used in Equation (14) it produces

$$s_{SWDn}(k, l) = W\left(\frac{nK}{T_{Pri}}\right) \times A(k) \times e^{i2\pi nKl} \tag{17}$$

From Equation (17), we read that every harmonic $s_{SWDn}(k, l)$ represents a constant with respect to the l -index, and thus is removed by the clutter filter as a direct current. Moreover, the condition $F_M = K/T_{Pri}$ can be easily implemented in a digital system where the signals originate from a common clock of period T_{ck} :

$$T_{Pri} = N_{Pri} \times T_{ck} \Rightarrow F_M = \frac{K}{N_{Pri} \times T_{ck}} \tag{18}$$

N_{Pri} is chosen to achieve the desired $T_{Pri} = N_{Pri} \times T_{ck}$, which typically ranges in 50 μ s–10 ms, then K is selected so that F_M is in the working region of the power switcher. This is an easy task, since F_M can be selected with a resolution of, at least, $1/0.1 \text{ ms} = 10 \text{ kHz}$.

Although this simple method removes the power switching noise from the Doppler image, it assumes that the power switcher works at constant frequency F_M . This is not the best condition with respect to EMI compliance certification tests, so its practical usefulness is limited.

3.2. Triangle-Modulated Frequency Noise

From Equation (17) we know that a signal whose harmonics are a multiple of $1/T_{Pri}$ is canceled by the clutter filter. The goal is to achieve this condition also for triangular modulation. The condition is expressed by

$$\text{RECTp}[\varnothing(n_a \times T_{Pri})] = \text{RECTp}[\varnothing(n_b \times T_{Pri})] \quad \forall n_a, n_b \in \mathcal{N} \tag{19}$$

Thus, similar to the previous section, we aim to find a suitable relationship among the several parameters present in Equation (11) and T_{Pri} so that Equation (19) is valid. The periodicity of Equation (19) requires the T_{Pri} to be a multiple of the frequency modulation period. Moreover, the T_{Pri} should include an integer number of pulse periods (although the periodic temporal lengths vary due to modulation). These two conditions are formally written as

$$T_{Pri} = \frac{N}{F_{Mod}}; \quad N \in \mathcal{N} \tag{20a}$$

$$\varnothing(T_{Pri}) = K_{\varnothing} \quad K_{\varnothing} \in \mathcal{N} \quad (20b)$$

Using Equation (20a) in Equation (11) results in $\varnothing_B(T_{Pri}) = 0$. Thus $\varnothing(T_{Pri}) = \varnothing_A(N)$ and the constraint Equation (20) can be rewritten as follows:

$$T_{Pri} = \frac{N}{F_{Mod}}; \quad N \in \mathcal{N} \quad (21a)$$

$$\frac{N}{F_{Mod}} \left(\frac{1}{2}F_M + \frac{1}{2}F_m \right) = K_{\varnothing}; \quad K_{\varnothing} \in \mathcal{N} \quad (21b)$$

In summary, the constraints in Equation (21) represent the relations among T_{Pri} , F_{Mod} , F_M and F_m that, when verified, allows the switching noise to be completely eliminated by the clutter filter applied before the spectral analysis in the Doppler processing. Moreover, these constraints are practically solvable with the typical parameter values used in Doppler investigations. For example, with $F_{Mod} = 10$ kHz, $T_{Pri} = 200$ μ s, and $N = 2$, Equation (21a) is valid; and $F_M = 2.0$ MHz, $F_m = 1.6$ MHz, $K_{\varnothing} = 360$ solve Equation (21b).

However, the implementation of Equation (21) in a digital system, where all frequencies and signals are synthesized from a common high-frequency clock, with period T_{ck} , imposes further limits. As we achieved for Equation (18), F_{Mod} is quantized to

$$T_{Pri} = N_{Pri} \times T_{ck} \Rightarrow F_{Mod} = \frac{N}{N_{Pri} \times T_{ck}} \quad (22)$$

4. Method Implementation in the Doppler System

4.1. Experimental Doppler System

The experiments were performed by employing an ultrasound system designed for Doppler industrial applications. Details of the system can be found in [8,21]. Here, a simplified description is reported for the reader's convenience, with particular emphasis on power regulation and distribution, since that part is involved in the presented work. Figure 1 reports a sketch of the power tree. The system is powered by an external 12–24 V source that feeds the LT3507 [22] step-down switching regulator produced by Linear Technologies Corp (Milpitas, CA, USA). The LT3507 includes three switchers that can be synchronized between 250 kHz and 2.5 MHz. The switching inductors, capacitors and filters are sized to work, nominally, at 1.8 MHz; however, variations of $\pm 10\%$ (i.e., between 1.6–2.0 MHz) are acceptable [10]. LT3507 is employed to produce 5.5 V, 3.3 V and 1.8 V. The 5.5 V is further filtered, reduced to 5.0 V by a low dropout (LDO), and used to power the analog section of the board. This includes the most sensitive devices, such as, for example, the input low-noise amplifier (LNA), the programmable gain amplifier (PGA) and the analog-to-digital converter (ADC). The other outputs of the power switcher (3.3 V and 1.8 V) are used for the digital section of the board that includes, for example, a field-programmable gate array (FPGA) of the Cyclone III family (Intel-Altera, San Jose, CA, USA), a bank of SDRAM memory and communications devices. Several EMI filters are used to reduce the switching noise of the step-down regulator conducted back to the main supply and forward to the system sections.

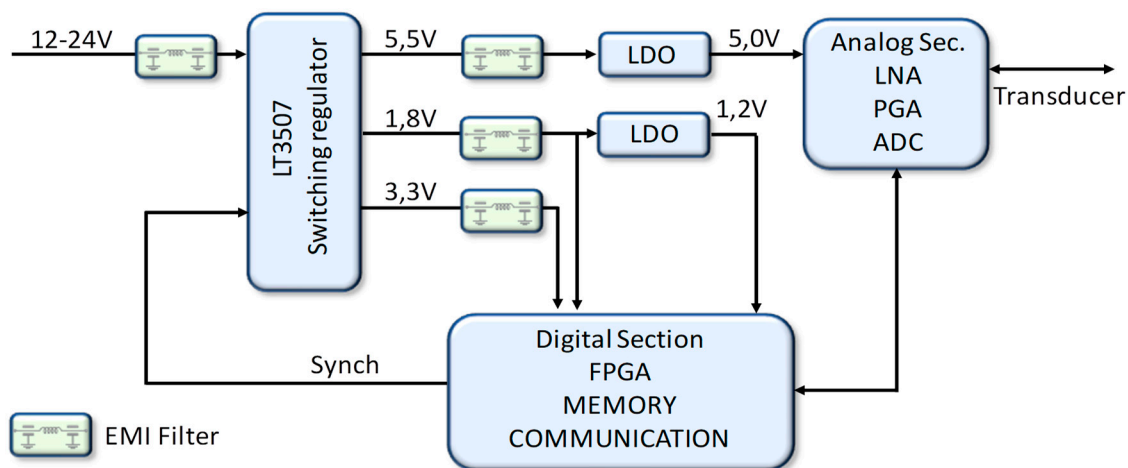


Figure 1. Simplified power tree of the Doppler system employed in the tests. The main switching regulator has three synchronous sections used to generate the powers for the analog and digital parts of the board. The regulator is synchronized by a signal from the local field-programmable gate array (FPGA). Electromagnetic interference (EMI) filters and further low dropouts (LDOs) are used at the input and outputs of the regulator.

The system features an input bandwidth from 0.1 MHz to 10 MHz, which is the typical range used in ultrasound applications in fluids; moreover, the LNA and PGA grant a gain up to 55 dB. The high gain and relatively large bandwidth make the input particularly sensitive to the noise.

The FPGA is in charge of the temporization of the system operations, the synthesis and the generation of the PRI sequence, of the signal acquisition and of the communication to the host. Moreover, the FPGA performs data processing in real-time following the steps reported in the previous sections. In this work the FPGA was further programmed to automatically calculate the parameters and generate the synchronization sequence for the step-down regulator as detailed in the next section.

4.2. Method Implementation in Hardware

The described method is implemented in the FPGA of the Doppler system, as sketched in Figure 2. The FPGA includes a NIOS II soft processor that manages the applications. Based on the T_{Pri} desired by the user, the processor calculates the integer $N_{Pri} = 100 \cdot \text{ROUND}(T_{Pri}/T_{ck}/100)$, where $\text{ROUND}(x)$ is the integer nearest to x . The desired T_{Pri} is thus approximated with the resolution $T_{ck} \times 100 = 1 \mu\text{s}$, which is sufficiently high for the application. Please note that N_{Pri} is divisible by 100. Next, the processor calculates F_{Mod} so that it is in the range of 10–20 kHz, and the condition in Equation (21a) is verified. The cases listed in Table 1 are used for the selection of the modulation frequency.

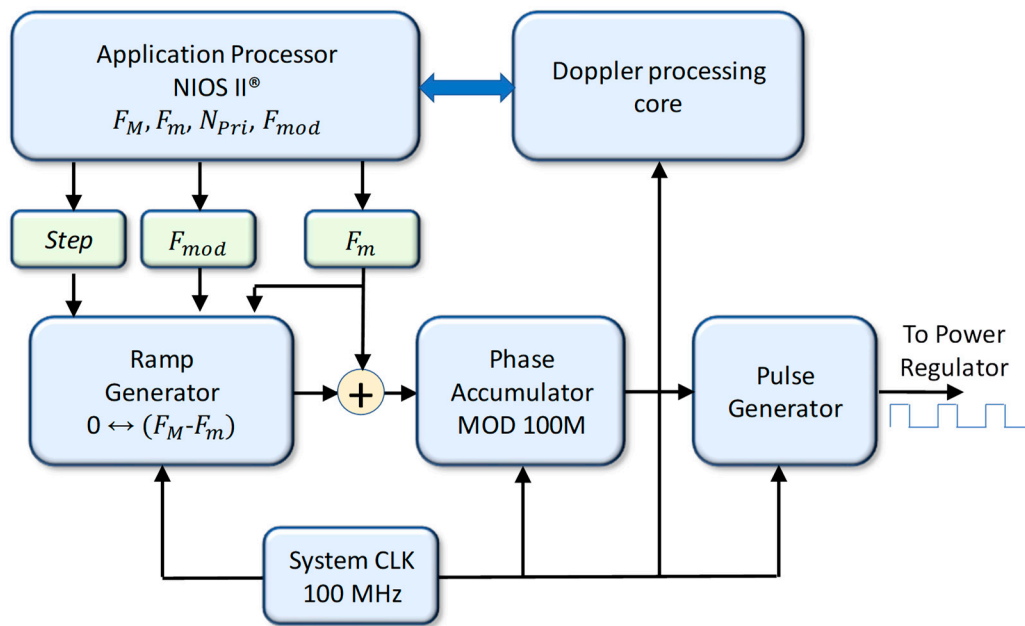


Figure 2. Method implementation in FPGA. The NIOS II soft processor calculates the $Step$, N_{Pri} , F_{Mod} , F_m and F_M parameters according to the reported constraints. $Step$, F_{Mod} and F_m are used by the ramp generators to produce a triangular wave of period $1/F_{Mod}$ and range $0 \leftrightarrow F_M - F_m$. The wave, added to F_m , enters an accumulator module 100 M. The phase is used for the synthesis of the synchronization pulse towards the switching regulator. The FPGA works with a 100-MHz clock.

Table 1. Selection of the frequency modulation F_{Mod} based on the N_{Pri} value.

$1/N_{Pri}$ Range	F_{Mod}
$10 \text{ kHz} < 1/N_{Pri} < 20 \text{ kHz}$	$F_{Mod} = 1/N_{Pri}$
$5 \text{ kHz} < 1/N_{Pri} < 10 \text{ kHz}$	$F_{Mod} = 2/N_{Pri}$
$4 \text{ kHz} < 1/N_{Pri} < 5 \text{ kHz}$	$F_{Mod} = 4/N_{Pri}$
$2 \text{ kHz} < 1/N_{Pri} < 4 \text{ kHz}$	$F_{Mod} = 5/N_{Pri}$
$1 \text{ kHz} < 1/N_{Pri} < 2 \text{ kHz}$	$F_{Mod} = 10/N_{Pri}$
$0.5 \text{ kHz} < 1/N_{Pri} < 1 \text{ kHz}$	$F_{Mod} = 20/N_{Pri}$
$0.4 \text{ kHz} < 1/N_{Pri} < 0.5 \text{ kHz}$	$F_{Mod} = 25/N_{Pri}$
$0.2 \text{ kHz} < 1/N_{Pri} < 0.4 \text{ kHz}$	$F_{Mod} = 50/N_{Pri}$
$0.1 \text{ kHz} < 1/N_{Pri} < 0.2 \text{ kHz}$	$F_{Mod} = 100/N_{Pri}$

Table 1 maps the ratios for the generation of the modulation frequency F_{Mod} to be used for T_{Pri} in the range of $100 \text{ Hz} < 1/N_{Pri} < 20 \text{ kHz}$, which is the frequency range used in the application of interest for the employed system. With the multiplication factors listed in Table 1, the condition in Equation (21a) is verified. In fact, N_{Pri} is rounded to 100 (see above), and thus is divisible by the 1, 2, 4, 5, 10, 20, 25, 50 and 100 factors listed in Table 1.

Once F_{Mod} is set, the processor calculates the minimum and maximum modulation frequencies F_m and F_M so that Equation (21b) is valid. These are approximated to frequencies 1.6 MHz and 2.0 MHz as follow:

$$F_m = \text{ROUND} \left(\frac{1.6 \times 10^6}{2 \times F_{Mod}} \right) \times 2F_{Mod} \tag{23a}$$

$$F_M = \text{ROUND} \left(\frac{2.0 \times 10^6}{2 \times F_{Mod}} \right) \times 2F_{Mod} \tag{23b}$$

The approximation is acceptable since the frequencies are not critical. The calculated values produce a modulation index of about $\pm 10\%$ with a central frequency of 1.8 MHz, which is the nominal frequency for the components (inductors, filter capacitors, etc.) used in the power supplier

included in the system. Next, the processor calculates how much the modulation frequency should be incremented/decremented for each clock cycle to generate the ramp up and down of the triangle modulation: $step = \frac{\Delta F_{Mod}}{T_C} = 2(F_M - F_m)/N_{Pri}$. This is a fractional value, and in the mathematics of the FPGA is represented with a precision of 10 fractional bits.

The F_m , $step$ and F_{Mod} feed the ramp generator implemented in the FPGA fabric (See Figure 2). The ramp generator increments/decrements its accumulator by $step$ every clock cycle, thus producing the triangle shape for the modulation in the range $0 \leftrightarrow (F_M - F_m)$. The ramp is added to F_m and integrated in the phase accumulator, which applies Equation (7a) and, every clock cycle, adds the input to the internal register. The accumulator works with a mathematics modulo 100 M (i.e., when the accumulator values passes 100 M, the module is subtracted to the accumulator). When this event occurs, a synchronization pulse is issued towards the switching regulator.

The circuit dedicated to synchronization, which includes the ramp generator, the phase accumulator and the pulse generator, is implemented in the FPGA fabric of the Cyclone III FPGA of the system with 97 adaptive look-up tables (ALUTs) and 34 registers only. Time closure was achieved for the 100-MHz clock.

5. Experiments and Results

5.1. MATLAB Simulations

The signal models proposed in Section 3 were first verified in MATLAB. In the presented simulations, both the simple constant-frequency and the triangle-modulated noise were tested. For each of the two modulation techniques, two sets of simulations were carried out. In the first set, the constraints in Equations (18) and (21) were not satisfied, so the presence of artifacts in the Doppler spectral matrices were expected. These simulations are considered as reference. On the other hand, the conditions in Equations (18) and (21) were satisfied by the second set of simulations, where Doppler spectral matrices were expected to be free from noise artifacts.

Table 2 lists the parameters used in the first set of simulations. The Doppler system was supposed to work with a clock at 100 MHz ($T_{ck} = 10$ ns). The power regulator switched at 2.0 MHz, and generated a fixed-frequency noise. The pulse repetition frequency (i.e., $1/T_{Pri}$) was about 7 kHz, obtained with 14,286 T_{ck} and corresponding to $T_{Pri} = 142.860$ μ s. The demodulator worked at 3.8 MHz, and the low-pass filter had $f_{LP} = 300$ kHz. In this setup, the condition in Equation (18) was not met, since the remainder of $T_{Pri}/(1/F_M) = 142.860 \cdot 2.0$ (i.e., it was not null).

Table 2. Parameters used in simulations when conditions for noise suppression were not met.

Parameter	No Modulation	Triangle Modulation
F_{Mod}	-	14.0003 kHz
T_{Pri}	142.860 μ s	142.860 μ s
F_m	-	1.6 MHz
F_M	2.0 MHz	2.0 MHz
F_d	3.8 MHz	3.8 MHz
f_{LP}	300 kHz	300 kHz
T_{ck}	10 ns	10 ns
N_{Pri}	14,286	14,286

Figure 3A shows the spectrum of the noise in dB normalized with respect to its maximum. Four harmonics are clearly visible in the lowest 10-MHz frequency span. The low-pass filter after the demodulator allowed the passage of the frequency range between 3.5–4.1 MHz (see Equation (15a)). This means that the f_{SW1} component of the simulated noise, placed at 4.0 MHz, passed through the filter. The harmonic was sampled at $1/T_{Pri}$, so, in the Doppler spectrum, it was located at $f_o = 3079.9$ Hz, where f_o is the remainder of $4.0 \text{ MHz}/(\frac{1}{T_{Pri}})$. Figure 3B shows the Doppler spectral matrix (i.e., Equation (14)) after spectral analysis has been performed along the l -index. In the figure, the k -index

is shown on the vertical axis (depth), while the horizontal axis represents the Doppler frequencies. The spectral power is coded in colors with rising brightness (black, red, yellow and white) for rising power. Figure 3C represents the Doppler spectral matrix averaged along the k -index. The amplitude is reported in dB normalized with respect to the maximum. As expected, a noise peak is clearly visible at $f_o = 3079.9$ in both panels.

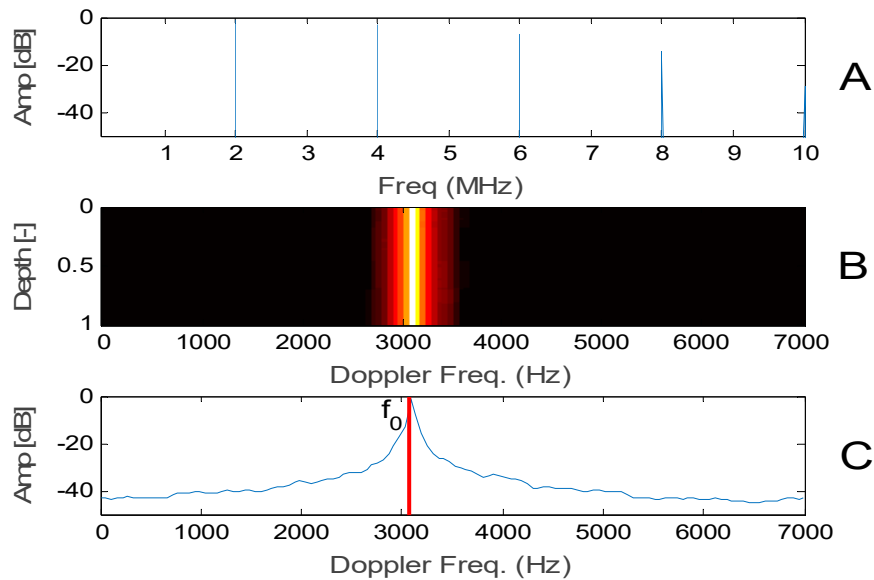


Figure 3. Simulation of the noise produced by a switching regulator working at 1.8 MHz in a Doppler system with $T_{Pri} = 142.86 \mu\text{s}$. (A) Spectrum of the noise as coupled to the input to the Doppler system; (B) Doppler spectral matrix; (C) spectral density averaged over depths (k -index). The condition in Equation (18) is not met, and a noise artifact is clearly visible at $f_o = 3079.9$ Hz.

In the second simulation, the triangle-modulated noise was calculated with the parameters listed in the right column of Table 2. The parameters were the same as used in the previous simulation, except for the modulation frequency F_{Mod} and the modulation range $F_m - F_M$. The modulation frequency was chosen exactly twofold the $1/T_{Pri}$ value, thus Equation (21a) is verified. However, the modulation range was between 1.6 MHz and 2.0 MHz, values that do not solve Equation (21b). An artifact noise is expected in the Doppler spectrum, and Figure 4A shows the spectrum of the noise in dB; the vertical axis has the same scale as Figure 2A to allow an easy comparison. As expected, the modulation spans the noise over the frequency range $F_m - F_M$ and the amplitude is correspondingly reduced. For example, the second group of harmonics, roughly located between 3–4 MHz, had a 20-dB attenuation with respect to simulation without modulation. The set-up of the demodulator was unchanged with respect to the previous simulation, so noise in the range of 3.5–4.1 MHz (see Equation (15a)) passed through the filter. As expected, an artifact was present in the Doppler spectral matrix (Figure 4B) and, correspondingly, in the mean spectrum obtained by averaging the matrix rows (Figure 4C). Note that although the modulation reduces the noise peak in the radio frequency (RF) spectrum (Figure 4A), a similar reduction is not present in the Doppler spectrum, where the peak reaches 0 dB as in Figure 3C.

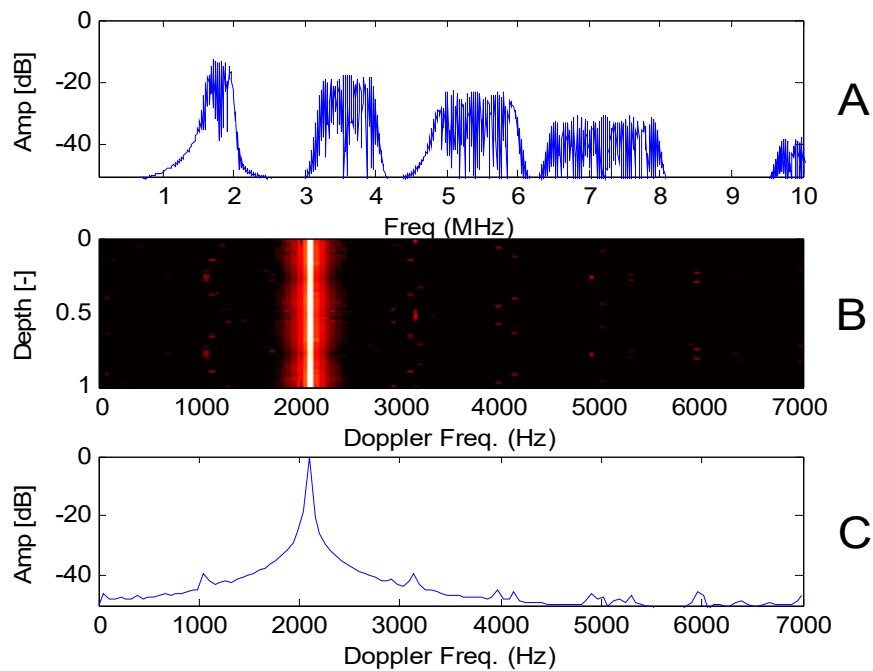


Figure 4. Simulation of the noise produced by a switching regulator modulated with a triangular frequency between 1.6–2.0 MHz in an acquisition with $T_{Pri} = 142.86 \mu s$. (A) Spectrum of the noise as input to the Doppler system; (B) Doppler spectral matrix; (C) spectral density averaged over depths (k -index). The constraint in Equation (21a) is verified, but Equation (21b) is not.

The simulations were repeated by changing the parameters as reported in Table 3. In the non-modulated noise simulation the F_M was unchanged, while the T_{Pri} was slightly modified to $143 \mu s$, verifying Equation (18). The RF spectrum of the noise (Figure 5A) was unchanged, but now the noise in the Doppler spectrum was moved at Doppler frequency 0, as shown in Figure 5B,C (the high-pass filter before the spectral analysis was removed just to better highlight the position of the noise).

Table 3. Parameters used in simulations where the conditions for noise suppression were met.

Parameter	No Modulation	Triangle Modulation
F_{Mod}	-	13.9860 kHz
T_{Pri}	143 μs	143 μs
F_m	-	1.5944 MHz
F_M	2.0 MHz	2.014 MHz
F_d	3.8 MHz	3.8 MHz
f_{LP}	300 kHz	300 kHz
T_{ck}	10 ns	10 ns
N_{Pri}	14300	14300

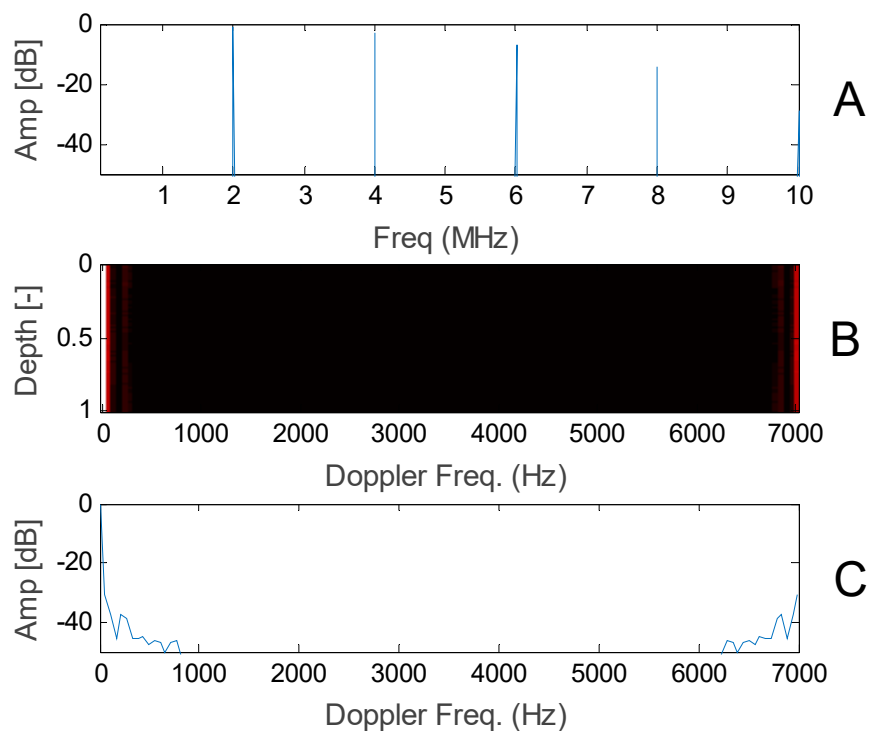


Figure 5. Simulation of the noise produced by a switching regulator working at 1.8 MHz in a Doppler system with $T_{Pri} = 143 \mu\text{s}$. **(A)** Spectrum of the noise as input into the Doppler system; **(B)** Doppler spectral matrix; **(C)** spectral density averaged over depths (k -index). The condition in Equation (18) is met, and artifacts due to noise are moved at frequency 0.

In the last simulation, the noise modulation was applied again. T_{Pri} was modified to $143 \mu\text{s}$, and the modulation frequency set to $F_{Mod} = 2/T_{Pri} \approx 13.986 \text{ kHz}$. The condition in Equation (21a) was verified. We further changed $F_M = F_{Mod} \times 144 \approx 2.014 \text{ MHz}$, and $F_m = F_{Mod} \times 114 \approx 1.594 \text{ MHz}$. Now Equation (21b) was verified by the values: $N = 2$ and $K_{\emptyset} = 258$. Results are reported in Figure 6. As expected, the RF spectrum is the same as in Figure 4A, but the noise artifact was moved at frequency 0 in the Doppler spectrum (here the clutter filter was removed to highlight the actual position of the noise).

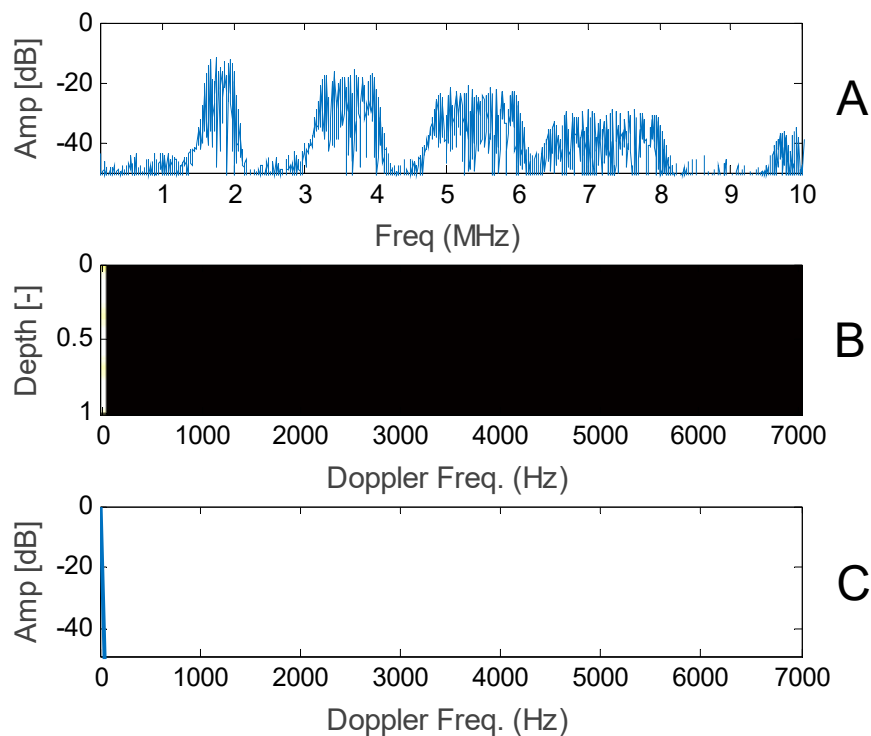


Figure 6. Simulation of the noise produced by a switching regulator modulated with a triangular frequency between 1.6–2.0 MHz, in an acquisition with $T_{pri} = 143 \mu\text{s}$. (A) Spectrum of the noise as input into the Doppler system; (B) Doppler spectral matrix; (C) spectral density averaged over depths (k -index). The constraints in Equation (21a) and Equation (21b) are verified, and artifacts are moved at frequency 0.

5.2. Measurements in Hardware

The measurements presented in this section were carried out on the Doppler system briefly introduced in Section 4. The measurements replicate the simulations presented in the previous section, and were obtained by employing the same parameters listed in Tables 2 and 3. In order to maximize the system susceptibility to noise, the input gain was set to its maximum of 55 dB, and the input was open. Both the RF signal (i.e., the signal acquired after amplification but before any processing) and the spectral matrices processed by the system were saved. Data were then reloaded in MATLAB to produce the figures presented in this section. In these experiments the clutter filter (100 Hz cut-off frequency) was active in the system and applied before spectral estimation.

The first measurements employed the parameters from Table 2 that did not verify the conditions in Equations (18) and (21b). To set these parameters it was necessary to disable the automatic procedure described in Section 4.2, where parameters were calculated by the application processor based on the desired T_{pri} for automatically verifying Equation (21). Thus, the automatic procedure was bypassed, and the processor was programmed exactly according to the parameters of Table 2. The results are reported in Figure 7, with the left and right columns for non-modulated and triangle-modulated noise, respectively. Figure 7A,D shows the RF spectrum. A background white noise is visible in within the bandwidth of the receiver (0.1–10 MHz). The background noise was set to a reference of 0 dB. With the switching-regulator synchronized to the fixed frequency of 2 MHz (Figure 7A), the harmonics of the switching noise are clearly visible at multiples of 2 MHz. On the other hand, measurements confirm that triangular modulation greatly reduced the switching noise in the RF spectrum, as shown in Figure 7D, where the switching noise is barely visible 2–3 dB over the background noise. Nevertheless, a noise peak is clearly visible in the color-coded Doppler spectral matrices (Figure 7B,E) and in the mean spectra (Figure 7C,F) in both non-modulated and modulated conditions. In these measurements,

the clutter filter was active (100 Hz cut-off frequency), and produced the darker region in the Doppler spectral matrices around frequency 0 and the corresponding amplitude reduction in the mean spectra.

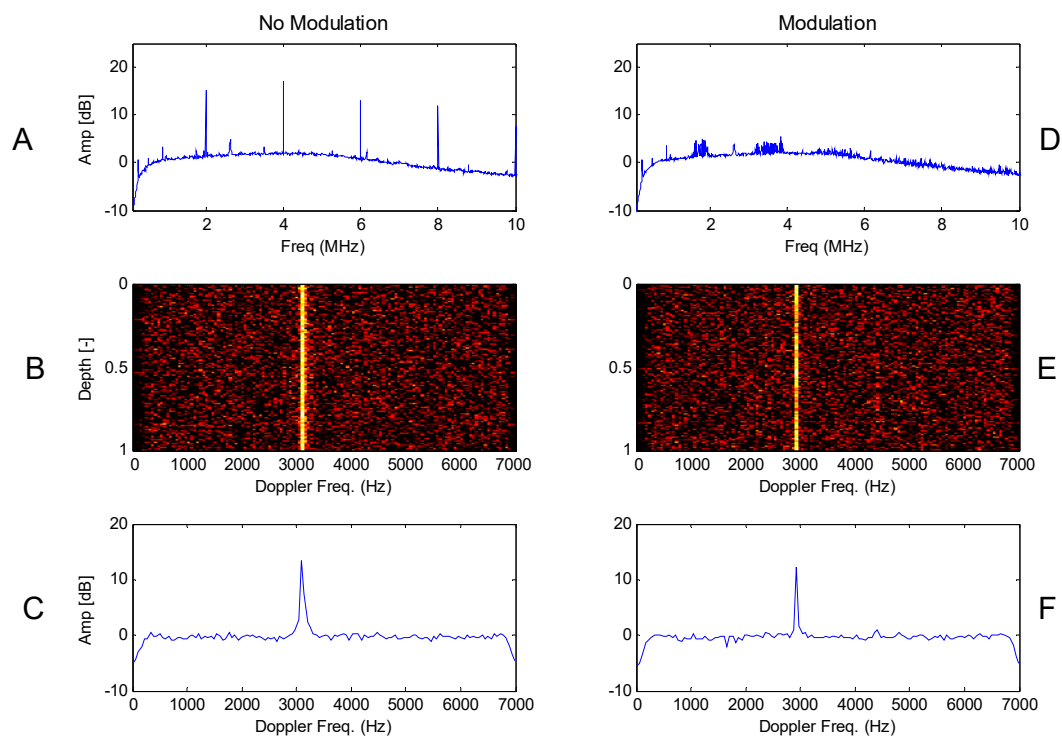


Figure 7. Measurements of the noise produced by a switching-regulator working at 1.8 MHz in a Doppler system with $T_{Pri} = 142.86 \mu\text{s}$. (A,D) Spectrum of the noise as input into the Doppler system; (B,E) Doppler spectral matrix; (C,F) spectral density averaged over depths (k -index).

The experiment was repeated with the parameters reported in Table 3, and the results are shown in Figure 8. As expected, the RF spectra are similar, but the switching noise is not visible in the Doppler spectral matrices (Figure 8B,E) and, correspondingly, in the mean spectra (Figure 8C,F), since it was completely removed by the clutter filter of the system.

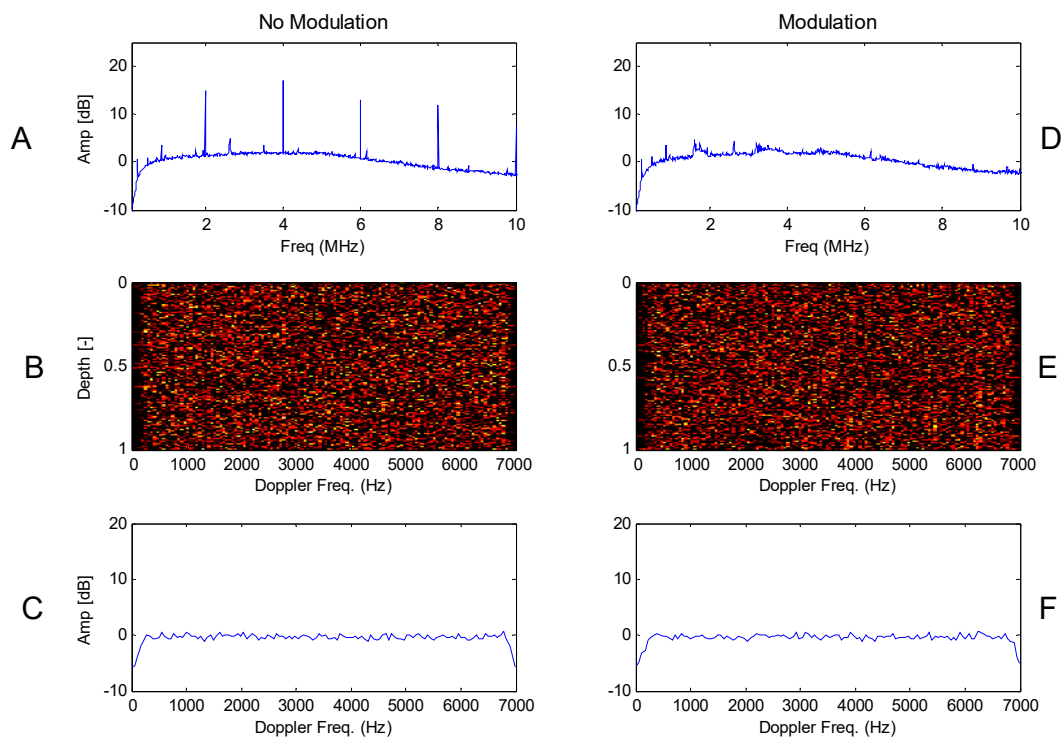


Figure 8. Measurements of the noise produced by a switching regulator working at 1.8 MHz in a Doppler system with $T_{Pri} = 143 \mu\text{s}$. (A,D) Spectrum of the noise as input into the Doppler system; (B,E) Doppler spectral matrix; (C,F) spectral density averaged over depths (k -index).

5.3. Flow-Rig Measurements

For the last experiment, the system was connected to an ultrasound transducer placed on a pipe with a 25.4-mm diameter [23]. The pipe was part of a laboratory flow-rig used for flow tests. The transducer was angled by 30° with respect to the pipe axis. A fluid composed of demineralized water with μ -metric plastic particles in suspension flowed in the pipe. These particles are used to produce ultrasound scattering, and a pump pushed the fluid at 0.4 m/s. In order to rise the susceptibility to noise, the transmission power was lowered so that it was necessary to rise the input gain to the maximum of 55 dB. The system excited the transducer by 3.8-MHz bursts of ultrasound every PRI, and processed the received echoes in real-time. The switching regulator was synchronized with triangular modulation. The experiment was repeated with the right-column parameters of Table 2 (i.e., with the constraint in Equation (21b) not verified) and with parameters of Table 3 (i.e., with the constraint in Equation (21b) verified). For this final experiment, the parameters were calculated by the automatic procedure described in Section 4.2. The measured color-coded Doppler spectral matrices are reported in Figure 9. In both circumstances, the system clearly detected the typical parabolic velocity distribution that a Newtonian fluid develops along the pipe diameter [24]. However, it is confirmed that when the constraints of Equation (21) are not met, annoying artifacts are visible in the Doppler spectral matrix (Figure 9A), while when Equation (21) is valid, the artifacts are removed (Figure 9B).

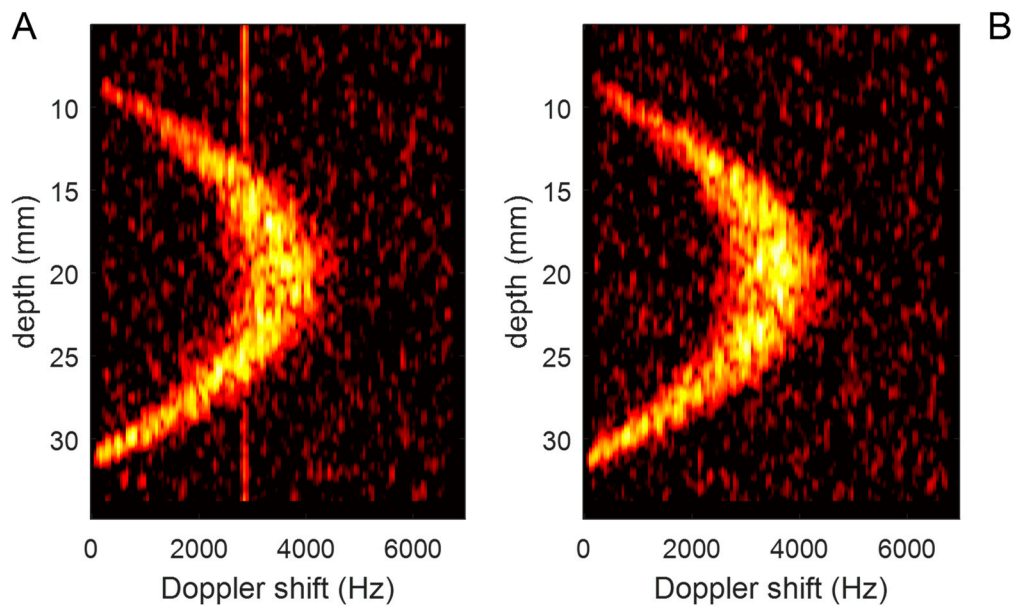


Figure 9. Doppler spectral matrices processed by the system when the power regulator is modulated by a triangle frequency. (A) Condition in Equation (21b) is not verified. (B) Condition in Equation (21b) is verified.

6. Discussion and Conclusions

The spread spectrum technique is an effective method for distributing the noise produced by switching regulators in wider spectral regions. The noise peak is consequently reduced and compliance to EMI certification limits is more easily achieved. Unfortunately, switching noise can produce annoying artifacts in Doppler applications even if spread spectrum is applied, as shown, for example, in Figure 4. In this work, a method for the efficient removal of noise produced by switching regulators is presented. The method is compatible with spread spectrum. In fact, it uses triangular frequency modulation, which is widely used in spread spectrum implementations [10] and tailors the modulation parameters on the specific Doppler application. The proposed method concentrates the noise in the small region of the Doppler frequencies that is cut by the clutter filter normally employed in Doppler applications. An implementation of the method in a Doppler system for velocity profile detection was detailed and tested in experiments. Although tests are reported for industrial applications, the proposed method can be applied to different applications, as in biomedical field [25,26].

Funding: This work is funded by the Ministero dell'Istruzione, dell'Università e della Ricerca (MIUR) of Italy Government with project PON AMICO ARS01_00900 CUP B56C18000710008.

Conflicts of Interest: The author declares no conflict of interest. The funders had no role in the design of the study; in the collection, analyses, or interpretation of data; in the writing of the manuscript, and in the decision to publish the results.

References

1. Evans, D.H.; McDicken, W.N. *Doppler Ultrasound Physics, Instrumentation and Signal Processing*; Wiley: Chichester, UK, 2000; ISBN 978-0471970019.
2. Ricci, S.; Ramalli, A.; Bassi, L.; Boni, E.; Tortoli, P. Real-Time Blood Velocity Vector Measurement over a 2-D Region. *IEEE Trans. Ultrason. Ferroelectr. Freq. Control* **2018**, *65*, 201–209. [[CrossRef](#)] [[PubMed](#)]
3. Fadnes, S.; Ekroll, I.K.; Nytnes, I.K.; Torp, H.; Løvstakken, L. Robust angle-independent blood velocity estimation based on dual angle plane wave imaging. *IEEE Trans. Ultrason. Ferroelectr. Freq. Control* **2015**, *62*, 1757–1767. [[CrossRef](#)] [[PubMed](#)]
4. Birkhofer, B.; Debacker, A.; Russo, S.; Ricci, S.; Lootens, D. In-line rheometry based on ultrasonic velocity profiles: comparison of data processing methods. *Appl. Rheol.* **2012**, *22*, 44701.

5. Wiklund, J.; Stading, M. Application of in-line ultrasound Doppler-based UVP–PD rheometry method to concentrated model and industrial suspensions. *Flow Meas. Instrum.* **2008**, *19*, 171–179. [[CrossRef](#)]
6. Kotzé, R.; Fester, V.; Kholisa, B.; Haldenwang, R.; Rössle, W. Commissioning of a novel in-line rheometry system in a wastewater treatment plant for more efficient polymer dosing. *Flow Meas. Instrum.* **2019**, *65*, 309–317. [[CrossRef](#)]
7. Neveu, F.; Allard, B.; Martin, C.; Bevilacqua, P.; Voiron, F. A 100 MHz 91.5% Peak Efficiency Integrated Buck Converter With a Three-MOSFET Cascode Bridge. *IEEE Trans. Power Electron.* **2016**, *31*, 3985–3988. [[CrossRef](#)]
8. Ricci, S.; Liard, M.; Birkhofer, B.; Lootens, D.; Brühwiler, A.; Tortoli, P. Embedded Doppler System for Industrial in-Line Rheometry. *IEEE Trans. Ultrason. Ferroelectr. Freq. Control* **2012**, *59*, 1395–1401. [[CrossRef](#)] [[PubMed](#)]
9. Zhu, H.; Liu, D.; Zhang, X.; Qu, F. Reliability of Boost PFC Converters with Improved EMI Filters. *Electronics* **2018**, *7*, 413. [[CrossRef](#)]
10. Balcells, J.; Santolaria, A.; Diez, D.G.; Gago, J.; Orlandi, A. EMI reduction in switched power converters using frequency Modulation techniques. *IEEE Trans. Electromagn. Compat.* **2005**, *47*, 569–576. [[CrossRef](#)]
11. Guo, H.; Wu, H.; Zhang, B.; Li, Z. A novel spread-spectrum clock generator for suppressing conducted EMI in switching power supply. *Microelectron. J.* **2010**, *41*, 93–98. [[CrossRef](#)]
12. Nguyen, V.H.; Huynh, H.A.; Kim, S.; Song, H. Active EMI Reduction Using Chaotic Modulation in a Buck Converter with Relaxed Output LC Filter. *Electronics* **2018**, *7*, 254. [[CrossRef](#)]
13. CISPR 11:2015. *Industrial, scientific and medical equipment—Radio-frequency disturbance characteristics—Limits and methods of measurement*, 6th ed.; International Electrotechnical Committee (IEC): Geneva, Switzerland, 2015.
14. Bjaerum, S.; Torp, H.; Kristoffersen, K. Clutter filter design for ultrasound color flow imaging. *IEEE Trans. Ultrason. Ferroelectr. Freq. Control* **2002**, *49*, 204–216. [[CrossRef](#)]
15. Ricci, S.; Meacci, V.; Birkhofer, B.; Wiklund, J. FPGA-based System for In-Line Measurement of Velocity Profiles of Fluids in Industrial Pipe Flow. *IEEE Trans. Ind. Electron.* **2017**, *64*, 3997–4005. [[CrossRef](#)]
16. Ricci, S.; Meacci, V. Data-Adaptive Coherent Demodulator for High Dynamics Pulse-Wave Ultrasound Applications. *Electronics* **2018**, *7*, 434. [[CrossRef](#)]
17. Cooley, J.W.; Tukey, J.W. An Algorithm for the Machine Calculation of Complex Fourier Series. *Math. Comput.* **1965**, *19*, 297. [[CrossRef](#)]
18. Ricci, S. Adaptive spectral estimators for fast flow-profile detection. *IEEE Trans. Ultrason. Ferroelectr. Freq. Control.* **2013**, *60*, 421–427. [[CrossRef](#)]
19. Elif, D.Ü.; Hakan, I.; İnan, G. Application of FFT and Arma Spectral Analysis to Arterial Doppler Signals. *Math. Comput. Appl.* **2003**, *8*, 311–318.
20. Larsson, E.G.; Stoica, P. Fast Implementation of Two-Dimensional APES and CAPON Spectral Estimators. *Multidimens. Syst. Process.* **2002**, *13*, 35–53. [[CrossRef](#)]
21. Meacci, V.; Ricci, S.; Wiklund, J.; Birkhofer, B.; Kotze, R. Flow-Viz - An integrated digital in-line fluid characterization system for industrial applications. In Proceedings of the 11th IEEE Sensors Applications Symposium (SAS), Catania, Italy, 20–22 April 2016.
22. Analog Devices. Available online: <https://www.analog.com/en/products/lt3507.html> (accessed on 11 March 2019).
23. Kotzé, R.; Ricci, S.; Birkhofer, B.; Wiklund, J. Performance tests of a new non-invasive sensor unit and ultrasound electronics. *Flow Meas. Instrum.* **2016**, *48*, 104–111. [[CrossRef](#)]
24. Granger, R.A. *Fluid Mechanics*; Dover: Mineola, NY, USA, 1995.
25. Ricci, S.; Matera, R.; Tortoli, P. An improved Doppler model for obtaining accurate maximum blood velocities. *Ultrasonics* **2014**, *54*, 2006–2014. [[CrossRef](#)]
26. Morganti, T.; Ricci, S.; Vittone, F.; Palombo, C.; Tortoli, P. Clinical validation of common carotid artery wall distension assessment based on multigate Doppler processing. *Ultrasound Med. Biol.* **2005**, *31*, 937–945. [[CrossRef](#)] [[PubMed](#)]

